UC Berkeley
UC Berkeley Previously Published Works

Title

Li—Mn—O Li-rich cation disordered rock-salt cathode materials do not undergo reversible oxygen redox during cycling

Permalink

https://escholarship.org/uc/item/0jp0n2bs

Journal

Journal of Materials Chemistry A, 11(42)

ISSN

2050-7488

Authors

Yin, Wei
Alvarado, Judith
Kedzie, Elyse A
et al.

Publication Date

2023-10-31

DOI

10.1039/d3ta04873j

Peer reviewed

Li-Mn-O Li-rich Cation Disordered Rock-salt Cathode Materials Do Not Undergo Reversible Oxygen Redox During Cycling

Wei Yin,[a] Judith Alvarado,[a] Elyse A. Kedzie,[a,b] Bryan D. McCloskey,[a,b] Chaochao Dun,[c] Jeffrey J. Urban,[c] Zengqing Zhuo,[d] Wanli Yang,[d] and Marca M. Doeff [a,*]

[a]*Energy Storage & Distributed Resources Division, Lawrence Berkeley National Laboratory, Berkeley, CA 94720, USA*

[b]*Department of Materials Science and Engineering, University of California Berkeley, Berkeley, CA 94720, USA*

[c]*The Molecular Foundry, Lawrence Berkeley National Laboratory, Berkeley, CA 94720, USA*

[d]*Advanced Light Source, Lawrence Berkeley National Laboratory, Berkeley, CA 94720 USA*

E-mail: mmdoeff@lbl.gov

Abstract

An in-depth study of "$Li_4Mn_2O_5$", a nanocomposite of Li_2O and $Li_{4-x}Mn_2O_5$ with a disordered rock salt structure (LMO), was conducted to determine the origins of the observed anomalously high charge and discharge capacity in lithium cells, which can exceed 350 mAh/g. Using soft and hard X-ray absorption spectroscopy (XAS), mapping of resonant inelastic X-ray scattering (mRIXS), and X-ray Raman spectroscopy (XRS), it was determined that electrochemical decomposition of Li_2O upon charge and reduction of Mn to below 3+ during discharge is responsible for the capacities that are observed, with no evidence of contributions from reversible oxygen redox. The over-reduction is exacerbated when charging limits of 4.5-4.8V are used due to side reactions between electrolytic solution and the highly oxidized active material. These side reactions result in dissolution of Mn at room temperature and release of oxygen and other gases during initial cycles, which, in turn, cause rapid capacity fading. This is accompanied by evolution of the voltage profile upon cycling towards one that resembles that of manganese oxide spinels. The cycling behavior can be improved somewhat by reducing the upper voltage limit, although this results in a diminishment of the discharge capacities below 200 mAh/g. By adding various amounts of spinel $LiMn_2O_4$ during synthesis, it was possible to produce LMOs with rock salt structures having significantly improved cycling behavior but still having capacities in excess of 250 mAh/g. An optimized modified material also exhibits better rate capability and much less gas evolution during initial cycles than the unmodified LMO. Interestingly, as-made modified materials generally exhibited lower than expected average Mn oxidation states attributable to oxygen loss during the synthesis process, as well as higher capacities than expected based on their manganese contents. The oxygen loss during processing may reduce the activity of the remaining oxygen and account for the lower reactivity of the spinel-modified material.

Introduction

Increasing concerns about sustainability and cost has prompted the electrochemical energy storage community to seek alternatives to the commonly used NMC ($LiNi_xMn_yCo_zO_2$; x+y+z≈1) cathode materials for Li-ion batteries.[1,2] Cobalt, in particular, is relatively scarce and expensive,

1

driving developers to decrease its content in NMC cathodes and to consider alternatives such as manganese oxide spinels,[3] lithium manganese-rich oxides (LMR)[4] and disordered rock salt (DRX)[5,6] materials, particularly compositions which avoid use of cobalt and nickel as well. In principle, electrode materials with manganese as the predominant transition metal are very attractive, based on the abundance and low cost of this element, but these have been plagued by short cycle lives due to manganese dissolution, oxygen loss, and structural rearrangement[7] hampering their commercialization for deployment in batteries.

Several years ago, Pralong et al.[8] reported on a material with an unusually high discharge capacity, termed "$Li_4Mn_2O_5$", made by reactive ball-milling. They later determined that "$Li_4Mn_2O_5$" was actually a nanocomposite of Li_2O and a disordered rock salt with composition $Li_{4-x}Mn_2O_5$, and that Li_2O was involved in the redox processes that lead to the high capacities.[9] The large capacities exhibited by other DRX compounds such as $Li_{1.3}Nb_{0.3}Mn_{0.4}O_2$[10] have been attributed to both transition metal redox and oxygen redox. The latter is only partially reversible, and results in capacity fade due to loss of oxygen and cation rearrangement at particle surfaces as well as over-reduction of transition metals at the surface and side reactions. Fluorination mitigates these processes to some extent, by reducing the oxygen activity, as evidenced by improved cycling in $Li_{1.2}Mn_{0.6}Ti_{0.2}O_{1.8}F_{0.2}$[11] and $Li_{1.2}Mn_{0.7}Nb_{0.1}O_{1.8}F_{0.2}$.[12] Even in the fluorinated compounds, spinel-like ordering has been observed in cycled DRX electrodes, indicating structural instability.[13,14,15]

Many DRX materials require charging to high voltages (4.8V vs. Li^+/Li or even higher) to activate oxygen redox and realize their full capacities. Under these conditions, electrolyte oxidation, with a concomitant rise in cell impedance, and even cell dry-out over the long term, are risks. Recent work has focused on the development of electrolyte additives and/or solvents that allow better high voltage and elevated temperature operation for cells containing conventional cathodes such as high Ni-content NMCs (NMC=$LiNi_xMn_yCo_zO_2$; x+y+z≅1).[16,17] These new formulations may mitigate some of the adverse effects of high voltage operation on DRX and related materials.

One objective of this work was to determine whether the origins of the anomalous capacity of "$Li_4Mn_2O_5$" can be partially attributed to oxygen redox, as is observed in many of the more compositionally complex DRX electrodes. For this, we used a suite of bulk and surface-sensitive X-ray techniques including X-ray absorption spectroscopy (XAS) and mapping of resonant inelastic X-ray scattering (mRIXS). For further background on these techniques, consult reference 18. A second goal was to understand the causes of capacity fading, and to reduce these using synthetic strategies. While fluorination showed some benefits, a more effective strategy appeared to be modification of lithium and manganese content by mixing in manganese oxide spinel during the high energy ball milling process used for synthesis. The best material made this way showed greatly improved cycling and rate capability properties and evolved significantly less oxygen upon the first cycle.

Experimental

Material Synthesis

$Li_xMn_yO_z$ materials were synthesized using a mechanochemical ball-milling method. Materials with the nominal composition of $Li_4Mn_2O_5$ were prepared by dry ball-milling a stochiometric mixture of Li_2O (Sigma Aldrich, ~ 60 mesh, 97%) with Mn_2O_3 (Sigma Aldrich, 99.9%) for 24 hours at 600 rpm. In some cases, 10% or 20% excess of Li_2O was used during the synthesis to study the effect of excess Li_2O on the electrochemical properties of $Li_4Mn_2O_5$. For some compositions, LiF was added in the desired quantities to form partially fluorinated compounds. In other cases, the powder made with a stoichiometric mixture was then milled with $LiMn_2O_4$ (NEI Corporation) in various molar ratios for 20 hours at 600 rpm. All mixtures were sealed in air-tight jars in an argon-filled glovebox with H_2O and O_2 less than 1 ppm. Milling was carried out in 5-minute intervals separated by 10-minute rests to avoid excessive heat generation.

Materials Characterization

Laboratory X-ray diffraction (XRD) patterns of the samples were recorded using a BRUKER D2 powder X-ray diffractometer equipped with Cu Kα radiation source ($\lambda_{K\alpha 1}$ = 1.5406 Å, $\lambda_{K\alpha 2}$ = 1.54439 Å, 40 kV, 30mA). *Ex situ* synchrotron XRD patterns were collected at beamline 2-1 of Stanford Synchrotron Radiation Lightsource (SSRL). Data was acquired in transmission mode using X-rays at 17 keV (λ = 0.729 Å) and a Pilatus 100K two-dimensional area detector with typical exposure time of 3 min. Powders were sandwiched in the argon-filled glovebox between two layers of Kapton tape for *ex situ* XRD experiments. Le Bail fitting was used to obtain lattice parameters. *Ex situ* Mn K-edge hard X-ray absorption spectroscopy (XAS) spectra were collected in transmission modes using a Si (220) monochromator at beamline 2-2 at SSRL. Calibration was applied to all spectra using the first inflection point of the corresponding Mn metal foil. *Ex situ* Mn L-edge and O K-edge soft XAS spectra were collected at beamline 10-1 at SSRL under ultrahigh vacuum (10^{-9} Torr) at room temperature using the total electron yield (TEY) detector. The measurements were conducted with a 31-pole wiggler and a spherical grating monochromator with 20 μm entrance and exit slits, providing a 0.2 eV energy resolution in a 1 mm^2 beam spot. X-ray Raman spectroscopy (XRS) experiments were conducted at beamline 6-2b of SSRL. The Mn L-edge and O K-edge were measured using the 40-crystal X-ray Raman spectrometer (with an energy resolution of ~0.45 eV using the Si(660) mode) and an incident X-ray beam of ~150 × 400 μm^2 monochromatized with a Si(311) monochromator. Mapping of resonant inelastic X-ray scattering (mRIXS) measurements were performed at the iRIXS end station at beamline 8.0.1 of the Advanced Light Source (ALS). Mapping data were collected by the ultra-high efficiency modular spectrometer with an excitation energy step of 0.2 eV. The resolution of the excitation energy was about 0.25 eV, and that of the emission energy was about 0.35 eV. Samples for mRIXS were transferred using a home-made sample handling kit that was sealed in the glovebox and coupled to the iRIXS vacuum system without any air exposure.

X-ray photoelectron spectroscopy (XPS) experiments were performed using a Thermo Scientific XPS instrument operating at a base pressure lower than $2 × 10^{-8}$ Torr using an Al Kα source (λ = 1487 eV). High-resolution spectra were recorded using a 50 meV pass energy over a

measurement spot of 400 μm. XPS peaks were fitted with a Gaussian–Lorentzian function. A combined low energy electron/ion flood source was used for charge neutralization. The gas cluster Argon ion source was used for depth profiling.

Differential electrochemical mass spectrometry (DEMS) experiments were carried out to quantify the gas evolution from $Li_xMn_yO_z$ electrodes during the initial two electrochemical cycles. DEMS cells were rested at open circuit voltage for 5 hours prior to the start of the galvanostatic cycling at a current rate of C/10. Gas evolution was monitored using a custom-built DEMS apparatus, as described in prior publications.[19] DEMS cell headspace was sampled every 10 min and any accumulated gases were swept to the mass spectrometer chamber. The amount of gas evolved was quantified using the volume and temperature of the gas sample.

Electrochemical Characterization

$Li_xMn_yO_z$ active materials were first milled with carbon (acetylene black) in a 7:2 weight ratio for 1 hour at 600 rpm and then mixed with poly(vinylidene fluoride) (PVDF) binder in N-methyl-2-pyrrolidone (NMP) solvent by mortar and pestle. The mass ratio of $Li_xMn_yO_z$, carbon, and PVDF is 7:2:1. The slurries were then cast onto carbon-coated aluminum foils. The electrodes were dried under vacuum at 120 °C for 12 hours before being cut to size and weighed. The typical electrode loadings were ~ 1.5 – 2.0 mg_{AM} cm^{-2}. 2032-type coin cells were assembled in an argon-filled glovebox with H_2O and O_2 less than 1 ppm using metallic lithium foil as counter electrodes, GF/F glass fiber (Whatman) separators, and electrolyte solution of 1 M Lithium hexafluorophosphate ($LiPF_6$) in ethylene carbonate/diethyl carbonate (EC/DEC = 1/1 (v/v)). Electrochemical measurements were performed using a VMP3 multichannel potentiostat/galvanostat (BioLogic) under ambient conditions at a current rate of C/20 unless otherwise stated, with C/20 being the current rate to extract/insert 1 Li^+ in 20 hours, *i.e.*, 4 Li^+ in 80 hours.

Results and Discussion

The targeted $Li_4Mn_2O_5$ material, denoted hereafter as LMO, was synthesized using a mechanochemical ball milling method, as detailed in the experimental section. The powder X-ray diffraction (XRD) pattern of the as-synthesized material (Figure S1) is indexed to a Fm-3m cubic rocksalt space group with cell parameter a = 4.1430(11) Å.

The electrochemical behavior of LMO electrodes was tested in 2032-type coin cells *versus* Li at a C/20 current rate (Figure 1 and Figure 2a). As typically reported for this material,[8, 9,20] a charge capacity of over 400 mAh g^{-1} and discharge capacity of over 300 mAh g^{-1} were obtained during the first cycle when cycled within the 4.8 – 1.5 V voltage range. The initial charge and discharge profiles are sloping, characteristic of DRX-type materials. The high initial energy density is negated by the continuous fade of charge and discharge capacity upon cycling (Figure 1b). We further investigated the electrochemical properties for the LMO electrodes by cycling over different voltage ranges (Figures 1 & 3). In general, a narrower voltage window led to lower initial capacities for both charge and discharge. Furthermore, when LMO electrodes were charged to 4.8 V and discharged to increasingly lower voltage cutoffs, the cells showed rather similar capacity fades, except for the 1.2 V cell which had faster capacity decay (upper panel in Figure 2b) and a

larger ΔV increase (Figure 2c & bottom panel in Figure 2b). ΔV is the difference between the average charge and discharge voltage on each cycle, where an increase in ΔV implies a rise in cell resistance (although this can be complicated by structural changes that modify the voltage profile). A similar cycling test was performed by charging the LMO electrodes to four different upper voltage cutoffs, and discharging to the same lower voltage cutoff of 2.0 V (Figure 3). The 4.0 V and 4.2 V cells had nearly no capacity decay over 25 cycles compared to their 4.5 V and 4.8 V counterparts, which lost about 25 % of their initial discharge capacity (upper panel in Figure 2e). Of note in the bottom panel of Figure 2e is the small change in ΔV after 25 cycles for all the four cells, suggesting that the growth of cell resistance is not the primary cause for the apparent capacity fade seen for 4.5 V and 4.8 V cells. The electrolytic solution used here was not specially formulated for high voltage operation, so that it is likely that some irreversible oxidation of electrolyte occurred for the cells operated to 4.5 or 4.8V. If severe, this would lead to increased cell resistance during cycling and eventual cell failure. However, the cycling conditions are such that relatively little time is spent at high potentials, so the impact of electrolyte oxidation appears to be fairly minimal. Many previous reports have shown that manganese-rich (Mn-rich) cathodes suffer from Mn dissolution at high voltages which causes cathode active material loss, electrolyte decomposition, and surface reconstruction, thus leading to cell capacity decay.[21,22,23,24,25,26] The Mn species dissolved from the cathode can also migrate through the electrolyte and deposit on the anode surface. An optical image of the lithium metal anode and separator recovered from a cycled cell made with an LMO electrode (Figure S2) shows obvious black deposits at the surface, suggesting Mn dissolution. Notable changes are also observed in the voltage profiles and differential capacity versus voltage (dQ/dV) plots, indicative of structural changes in LMO electrodes, especially those subjected to high voltage conditions. There is a general trend of flattening of the initially sloping voltage profiles near 3 V upon cycling (Figures 1a – 1c and 3a-c), as also shown by the intensified redox peaks at approximately 3 V in the dQ/dV plots (Figures 1d – 1f and 3a-c). This occurs to a larger extent for the cells charged to 4.5 V or 4.8 V compared to the 4.0 V and 4.2 V counterparts. Moreover, a short plateau developed near 4 V upon cycling in the 4.5 V and 4.8 V cells, although it is absent in the 4.0 V and 4.2 V cells (Figures 1 & 3). This 4 V feature is similar to the 4 V plateau observed as LMR electrodes structurally transform during cycling [27] or in materials evolving spinel-related local structures.[1]
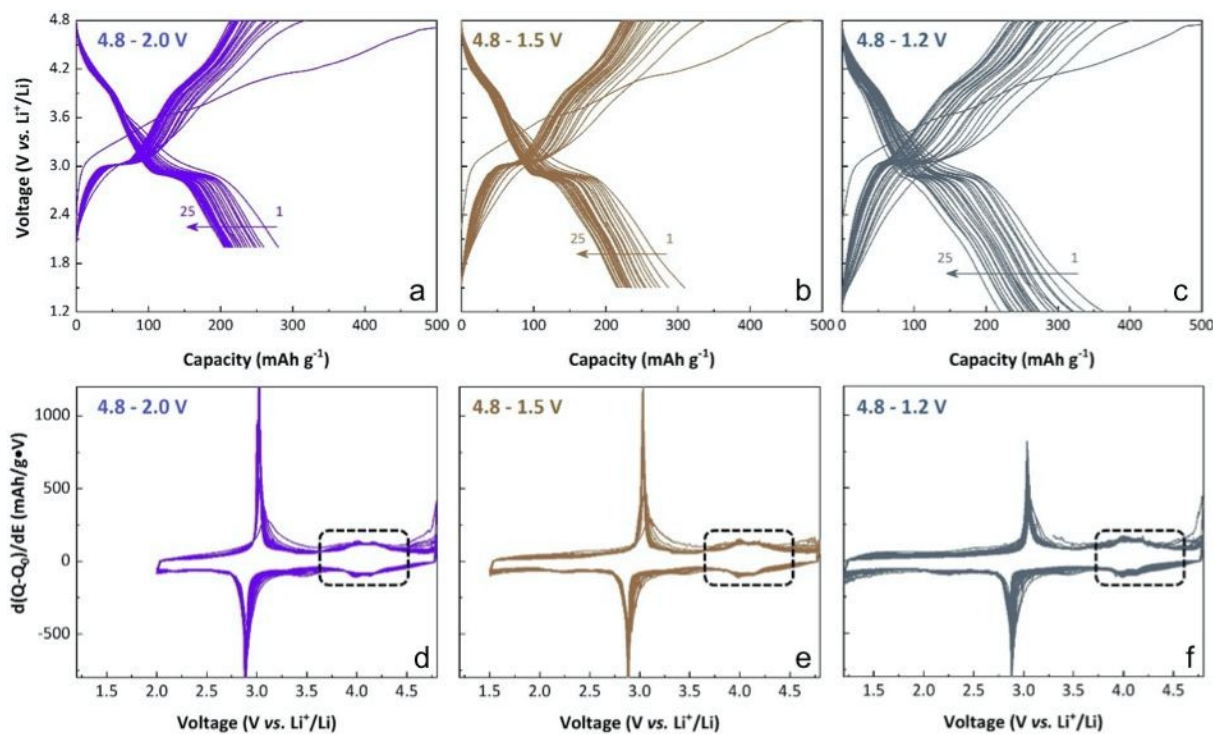
Figure 1 (a-c). Charge and discharge voltage profiles over 25 cycles and (e-h) the corresponding dQ/dV curves ($2^{nd} - 24^{th}$ cycles) for LMO electrodes charged to 4.8 V and discharged to the indicated lower cutoff limits. All the cells were cycled at current rate of C/20.
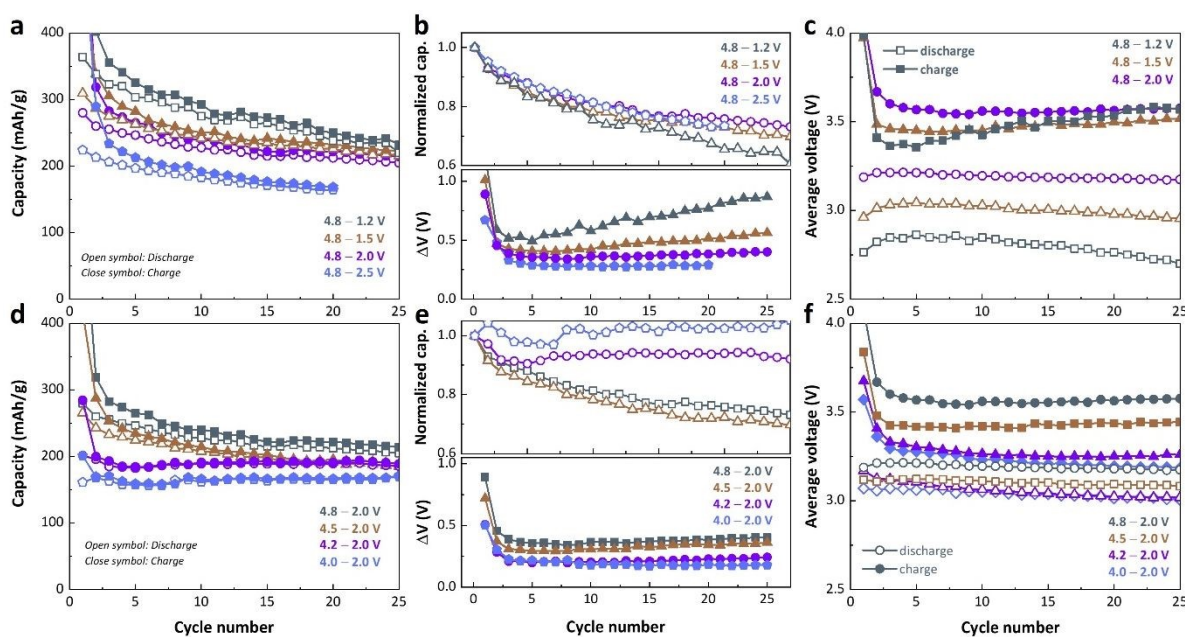

Figure 2. (a) Discharge and charge capacity retention, (b) normalized discharge capacity (upper panel) and ΔV (bottom panel), (c) average discharge and charge voltage of lithium-ion half-cells made with LMO electrode charged to 4.8 V and discharged to the indicated lower cutoff limits

over the initial 25 cycles. (d) Discharge and charge capacity retention, (e) normalized discharge capacity (upper panel) and ΔV (bottom panel), (f) average discharge and charge voltage of lithium-ion half-cells made with LMO electrode discharged to 2.0 V and charged to the indicated upper cutoff limits over the initial 25 cycles. ΔV is the difference between the average charge and discharge voltage of the cell. The average charge/discharge voltage is calculated from specific charge/discharge energy divided by specific charge/discharge capacity.
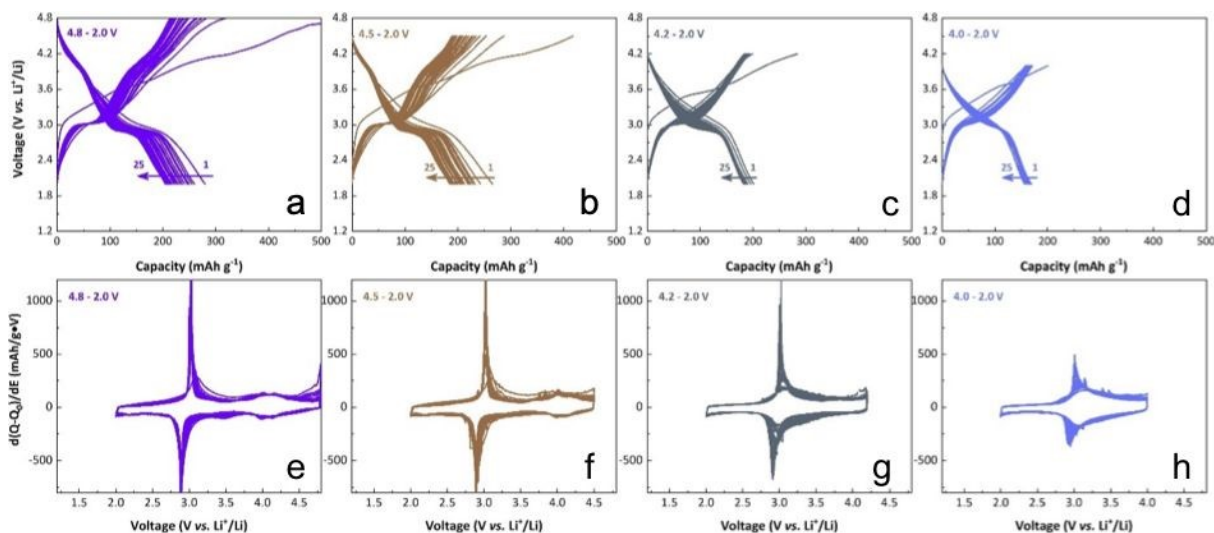
Figure 3. (a-d) Charge and discharge voltage profiles over 25 cycles and (e-h) the corresponding dQ/dV curves (2nd – 24th cycles) for LMO electrodes charged to the indicated upper cutoff limits and discharged to 2.0 V. All the cells were cycled at current rate of C/20.

Next, e*x situ* X-ray absorption spectroscopy (XAS) was performed at the Mn K-edge in transmission mode to probe the redox activities of Mn in the bulk material upon cycling (Figure 4). The absorption edge of pristine LMO is located at a similar position to Mn_2O_3, suggesting an oxidation state close to 3+. After removal of 2 Li^+ after charging to 4.0 V, the edge position shifts to a higher energy similar to that of MnO_2. The adsorption edge shows no further change upon charge to 4.2 V, but there is a slight shift towards lower energy for electrodes charged to 4.5 V and 4.8 V, suggesting Mn^{3+}/Mn^{4+} oxidation as the main charge contributor in the low voltage region and alternative mechanisms involving Mn reduction in the high voltage region. These could include side reactions involving electrolyte oxidation or oxygen release as discussed later. This is further supported by the evolution of the pre-edge regions shown in Figure 4b. The pre-edge feature of pristine LMO is characterized by a splitting of the Mn 3d orbitals into t_{2g} and e_g components. The position clearly shifts towards higher energy after the electrode is charged to 4.2 V, but then stops changing after further charging. *Ex situ* X-ray Raman spectroscopy (XRS) was also performed in parallel to provide complementary information on the variations of chemical states of Mn in the bulk. XRS is an energy loss spectroscopy that uses soft X-rays instead of electrons. It probes the bulk and provides information much deeper than that from equivalent to soft XAS in fluorescence yield (FY) mode, while avoiding the saturation effects. [28, 29] Figure 4c show the XRS spectra at the Mn L-edge for LMO electrodes at various states of charge. Based on the changes seen in the L_3 region, it is apparent that Mn^{3+} present in the pristine material is oxidized

to the tetravalent state on charging to 4.25 V but is not further oxidized during charge to 4.8V. This confirms the hard XAS results showing that the capacity obtained above 4.25 V is not charge compensated by Mn oxidation past the tetravalent state. In addition to the bulk Mn behaviors probed by hard X-ray XAS and XRS, the surface Mn states are characterized by Mn L-edge soft XAS in total electron yield (TEY) mode with a probe depth of about 10 nm. Surface Mn in LMO undergoes oxidation from Mn^{3+} to Mn^{4+} on charging to 4.2 V (Figure 4d). However, mixed states of Mn^{3+} and Mn^{4+} species appear in electrodes charged to 4.5 V and 4.8 V, in agreement with the hard XAS results and confirming the occurrence of surface Mn reduction.
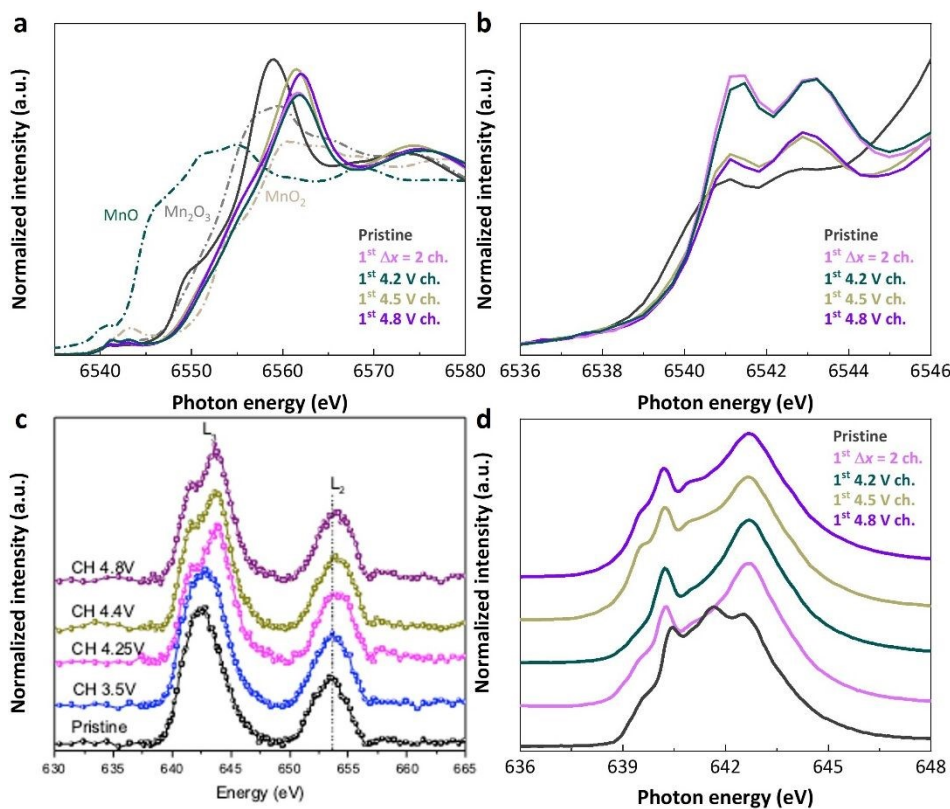
Figure 4. Normalized Mn K-edge hard XAS spectra of LMO electrodes charged to the indicated limits. Spectra obtained for MnO, Mn_2O_3 and MnO_2 standards are also shown in (a) as references. (b) shows the expanded view of the pre-edge regions. Δx is the amount of Li^+ removal. (c) *Ex-situ* hard XRS at Mn L-edge and (d) *ex situ* Mn L_3-edge soft XAS spectra in the total electron yield (TEY) mode for LMO electrodes charged to the indicated limits.

Some previous studies have postulated that oxygen redox may be responsible for some of the charge compensation, based either on Mn K-edge XAS and $K\beta_{1,3}$ X-ray emission spectroscopy (XES)[30] or O K-edge XAS results.[20] Although intriguing, these results suffer from the technical limitations of Mn K-edge XAS and $K\beta_{1,3}$ XES experiments, and the overwhelming effect of transition metal-oxygen (TM-O) hybridization in O K-edge XAS data.[31] Herein, complementary *ex situ* XRS, *ex situ* soft XAS, and mapping of resonant inelastic X-ray scattering (mRIXS) were used to probe the changes of the electronic structure of the oxygen ion and its bonding characteristics with the Mn ions. Figure 5 shows the *ex situ* hard XRS and soft XAS spectra at the

O K-edge for LMO electrodes at various states of charge. Soft XAS spectra were collected in both FY (Figure 5b) and TEY (Figure 5c) modes, providing information about the surface and into the bulk, respectively. All of the O K-edge spectra consist of a pre-edge region (< 535 eV) associated with the O1s transition to TM3d-O2p hybridization states and a higher energy region (> 535 eV) originating from O 1s transitions to hybridized TM4sp-O2p states. O-K edge XAS spectra of the pristine material exhibit two distinct peaks in the pre-edge region. The second peak is less apparent in the O-K edge XRS spectra due to the lower signal-to-noise ratio of XRS, because X-ray Raman cross sections are up to five orders of magnitude weaker compared to direct XAS. Of note is an additional peak centered at ~ 533 eV (Figure 5) with its intensity being the strongest in the O-K edge TEY XAS spectra (Figure 5c). This peak can be assigned to the oxygen in residual Li_2O. Li_2O is also observed in the synchrotron XRD pattern of LMO made with a stoichiometric amount of Li_2O (Figure S7) although not in the laboratory patterns (Figure S1). Some contributions from oxygen in Li_2CO_3 are also possible especially at the surface, considering that Li_2CO_3 has a sharp pre-edge feature at similar energies as Li_2O.[32] This peak completely disappeared after electrodes were charged to voltages above 3.5 V, indicating that the electrochemical decomposition of Li_2O and Li_2CO_3, which often takes in Li-rich compounds and can contribute significantly to the first-cycle charge capacity.[35] We intentionally synthesized materials with 10 % and 20 % excess of Li_2O and then assembled cells to evaluate the effect of excess Li_2O on the cell capacities. The initial charge capacity increases with excess lithia, but the initial discharge capacity remains largely unaltered (Figure S3). Other notable changes in the pre-edge features are a position shift to lower energy and an intensity increase for the LMO electrode charged to 4.0 V, suggesting increased Mn−O covalency, consistent with the observation of Mn oxidation from the Mn K-edge hard XAS results. Electrodes charged above 4.0 V had similar peak positions although there is a continuous increase in the peak intensities in O-K edge TEY XAS spectra. O-K XAS pre-edge variations in battery cathodes are dominated by changes of TM-d states and primarily probe the covalency of TM-O bonds.[33] In contrast, O-K mRIXS directly probes oxidized oxygen redox states through a sharp feature at 523.7 eV emission energy and/or low-energy loss features, different from that of the broad TM-O hybridization feature at 525 eV emission energy.[31][34] However, the O-K mRIXS image of the LMO electrode charged to 4.8V does not exhibit the telltale oxidized oxygen feature at an excitation and emission energy of 531.0 eV and 523.7 eV, respectively, indicating that any reversible oxygen redox if it occurs, is not detectable by mRIXS (Figure S4). Note that any trapped molecular oxygen, as recently proposed, should lead to these sharp RIXS features, and no evidence has been observed in a related system.[35]
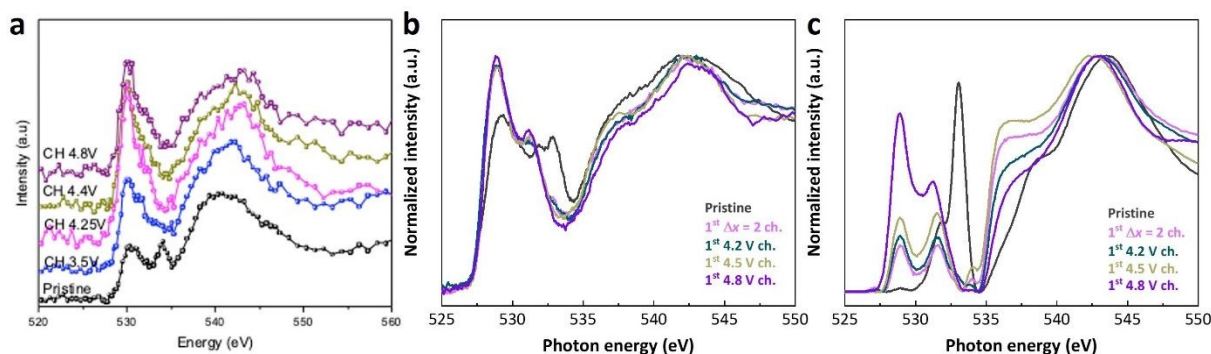
Figure 5. *Ex-situ* hard XRS at (a) O *K*-edge and *ex situ* O *K*-edge soft XAS spectra in the (b) fluorescence yield (FY) mode and (c) total electron yield (TEY) mode for LMO electrodes at the indicated states of charge.

Figure 6 compares Mn K-edge XAS, Mn L-edge XAS and O K-edge data in both FY and TEY modes on LMO electrodes in the pristine and discharged states, after initial charging to 4.8V. The Mn K-edge and L-edge results are consistent with reduction below the initial trivalent state for the electrodes discharged to 2.0V and 1.5V, as evidenced by the shifts to lower energies. This occurs not only at the surface (Figure 6b) but throughout the bulk (Figure 6a). The O K-edge data shows shifts consistent with changes in Mn-O covalency upon reduction of Mn, and the loss of surface Li_2O and Li_2CO_3 after the electrodes are charged (Figure 6d). In particular, we note that a significant amount of Mn^{2+} has formed on the surface after the discharge, indicated by the strong low energy peak in Mn-*L* TEY spectra in contrast to the pristine surface.[36]
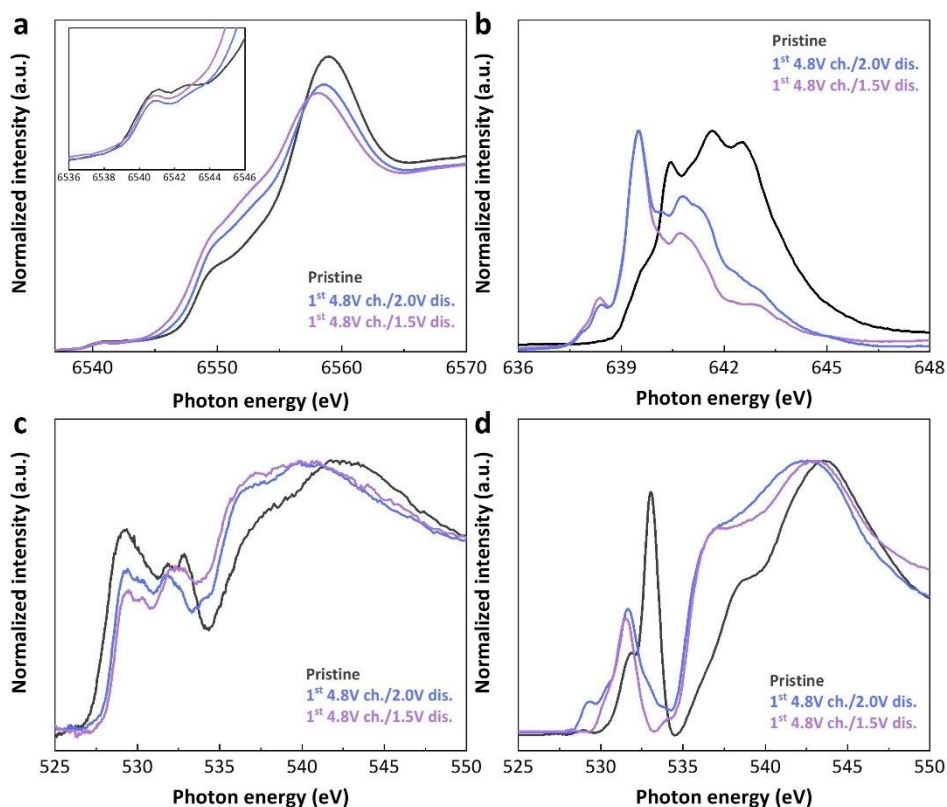

Figure 6. (a) Normalized Mn *K*-edge hard XAS, (b) Mn *L*-edge soft XAS spectra in TEY mode, and *ex situ* O *K*-edge soft XAS spectra in the (c) fluorescence yield (FY) and (d) total electron yield (TEY) mode of LMO electrodes at the indicated states of discharge. The sharp peak located at *ca.* 533 eV in (d) is attributed to signals from surface Li_2O and Li_2CO_3.
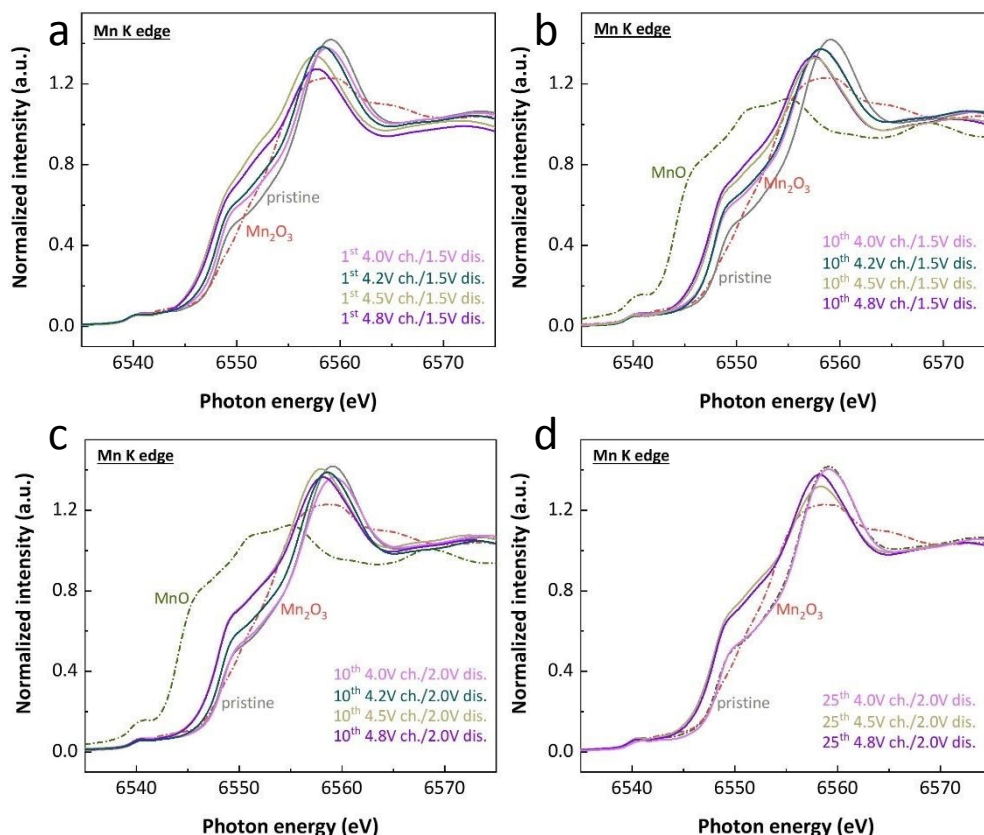
Figure 7. Normalized Mn *K*-edge hard XAS spectra of LMO electrodes charged to the indicated voltage and discharged to 1.5 V (a) during the initial cycle, (b) after 10 cycles, or discharged to 2.0V (c) after 10 cycles and (d) after 25 cycles. Spectra obtained for Mn_2O_3 and MnO standards are also shown as references.

Figure 7 shows Mn K-edge XAS data for LMO electrodes in the 1st, 10th, and 25th discharged state after cycling between various limits, along with MnO and/or Mn_2O_3 reference spectra. It is clear from these data that the average Mn oxidation state drops below +3 at the end of discharge when higher upper voltage limits of 4.5 or 4.8V are used to charge electrodes, and to a much lesser extent for electrodes cycled to lower charge limits of 4.0 or 4.2 V (Figure 7). When using a fixed charge limit (Figure 6a, Figures 7b & 7c), a larger amount of Mn^{3+} reduction is observed when discharged to 1.5 V than 2.0 V. The absolute values of Mn valence distributions at different electrochemical states can be directly quantified through a linear combination fitting of the $Mn^{2+/3+/4+}$ reference spectra (but see note 1 in supplementary section).[37,38] Table 1 lists these values for selected electrodes as well as the first cycle discharge capacity expected if only Mn redox is taken into account, assuming that Mn is fully oxidized to the tetravalent state at the top-of-charge when electrodes are charged above 4.2V. In most cases, the experimentally obtained values match surprisingly well with the calculated capacities, considering complications from side reactions and the observed Mn dissolution that occurs. Figure 8 compares the Mn K-edge (top) and Mn L-edge XAS (bottom) data for LMO electrodes in the discharged state after cycling between either 4.2-2.0V or 4.8-2.0V, as a function of cycle number. Insets show estimated

1

proportions of Mn^{2+} and Mn^{3+} for the discharged electrodes. There is a larger amount of Mn^{2+} when LMO electrodes are repeatedly charged to 4.8V compared to 4.2V (Figure 8b). More interestingly, the most significant Mn overreduction in the bulk occurs in the first cycle; only a small increase in Mn^{2+} content is observed with cycle number (Figure 8a). Consistently, the surface sensitive Mn-*L* XAS TEY (Figure 8c) displays dominant Mn^{2+} peaks right after the first discharge, which remains strong over extended cycles.[36] Similarly, Mn on the surface appears to be reduced on the first cycle, but there is no further shift to lower energies upon cycling whether 4.8 or 4.2V is used as the upper voltage limit (Figure 8c).

Overall, all the X-ray spectroscopic results together show that the anomalous capacity exhibited by the LMO electrodes can be explained by electrochemical decomposition of Li_2O or Li_2CO_3 upon the initial charge followed by Mn overreduction to lower than 3+ during discharge. Afterwards, Mn redox ($Mn^{2+}/Mn^{3+}/Mn^{4+}$) contributes to the capacity during the following charge and discharge without the need to invoke significant reversible O redox. Interestingly, a recent study on Li_2MnO_3[39] also reached a similar conclusion. These results imply that the presence of other transition metals in addition to manganese is necessary to induce reversible O-redox processes in oxide electrode materials.

Table 1. Calculated Mn oxidation states from hard XAS at the end-of-discharge and calculated and experimentally observed first discharge capacities.

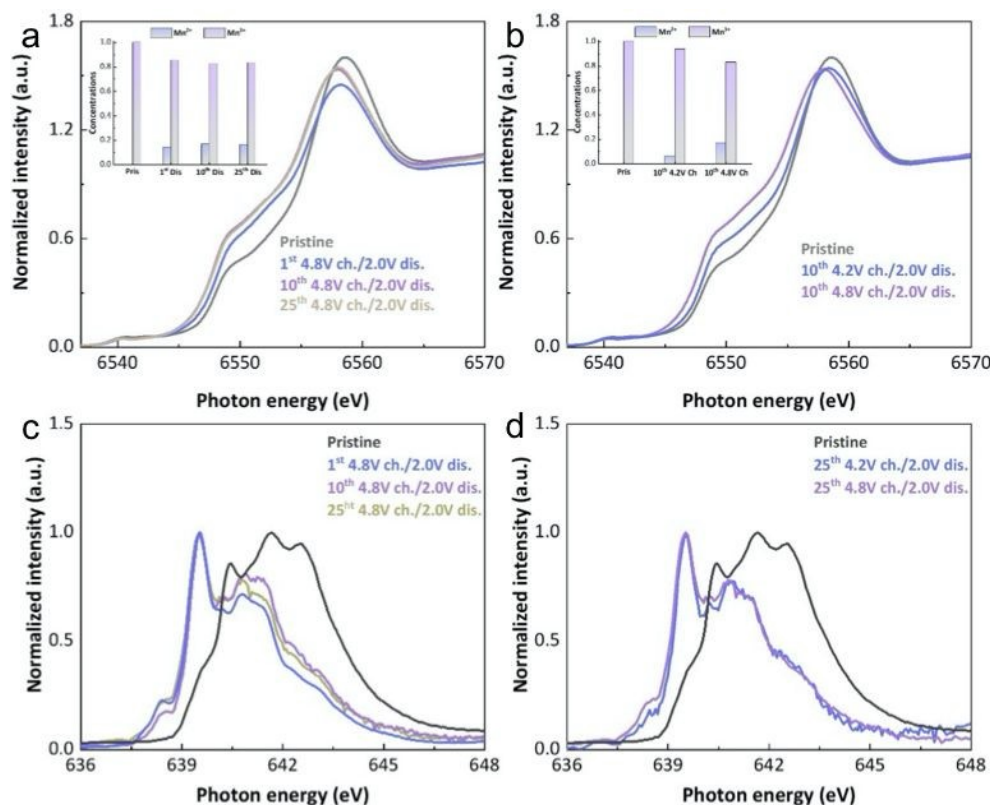| Conditions (1st cycle, voltage limits, V)	Mn oxidation state from XAS	Calculated Mn redox capacity (mAh/g)	Experimentally observed 1st discharge capacity (mAh/g)
4.8-2.0	+2.858	281.2 (2.284 e⁻)	280
4.8-1.5	+2.728	313.2 (2.544 e⁻)	309.2
4.8-1.2	+2.635	324.5 (2.73e⁻)	363.9
4.5-2.0	+2.825	289.3 (2.35 e⁻)	265.3
4.5-1.5	+2.72	315.2 (2.56 e⁻)	305
4.5-1.2	+2.636	335.9 (2.728 e⁻)	346.3

Figure 8. Normalized Mn K-edge hard XAS spectra of LMO electrodes (a) cycled to the indicated number of cycles within the 4.8 - 2.0 V voltage range; and (b) after 10 charge-discharge cycles within the voltage range of 4.8 - 2.0 and 4.2 - 2.0 V. Insets show the concentrations of Mn^{2+} and Mn^{3+} derived from Mn K-edge hard XAS spectra shown in (a) and (b), respectively. Mn L-edge soft XAS spectra in TEY mode of LMO electrodes (c) cycled to the indicated number of cycles within the 4.8 - 2.0 V voltage range; and (d) after 25 charge-discharge cycles within the voltage range of 4.8 - 2.0 and 4.2 - 2.0 V.

Depth-profiling C$1s$ and P$2p$ X-ray photoemission spectroscopy (XPS) was used to investigate the chemical composition of the interface between electrolyte and the LMO electrode charged to 4.8V (Figures S5a and S5b). Also shown are the C$1s$ and P$2p$ XPS surface data for a pristine electrode soaked in electrolyte as well as those for one that was charged, another that was discharged, and one discharged 25 times (Figures S5c and S5d). In the C$1s$ spectra, a signal due to Li_2CO_3 at ~ 290 eV is observed on the surface of the pristine electrode as well as that of the charged electrode (Figure S5c). For the pristine material, this probably arises from the chemical reaction of Li_2O with CO_2 upon air exposure, while decomposition of electrolyte may account for its presence in the charged electrode. As the etching time increased for the depth profiling experiment on the charged electrode (Figure S5a), the signal due to Li_2CO_3 gradually weakened, indicating these by-products are concentrated on the surface. $Li_xPF_yO_z$ decomposition products of $LiPF_6$ at ~ 135 eV, are also evident on the surfaces of the charged, discharged, and cycled electrodes, but absent in the P$2p$ spectrum of the pristine electrode (Figure S5d). Signals due to

alkyl carbonates are evident on the surfaces of all the electrodes. These results suggest that side reactions involving electrolytic solution occur, especially when cells are charged to high potentials. The products of these side reactions, which accumulate at the electrode surfaces contribute to the observed increase in cell impedance and apparent capacity fading upon cycling when a high charge limit of 4.8 V is used.

Based on previous reports of improved cycling for fluorinated DRX materials compared to the non-fluorinated analogs, we synthesized several modified LMOs by incorporating LiF during the reactive ball-milling process. XRD patterns of $Li_4Mn_2O_{5-x}F_x$; $x = 0.25$-1 are shown in Figure S6a. Results are consistent with rock salt structures for all the materials. Note that it is difficult to determine from the XRD results whether all of the fluorine is incorporated into the bulk or is present on surfaces (or both) since oxygen and fluorine have similar ionic radii.[40] Figure S6b shows cycling data for cells containing the fluorinated electrodes and unmodified LMO, charged and discharged between 4.8-1.5V at C/20 rate. Fluorination resulted in a modest improvement in capacity retention for some of the cells, although initial capacities were lower, roughly in proportion to the fluorine content. Figures S6c and S6d show voltage profiles and differential capacity plots for a cell containing $Li_4Mn_2O_4F$, which showed the most improvement over LMO, although capacity fading is still evident.

We also tried another synthetic approach, influenced by reports of synergistic effects when different cathode materials are blended together.[41] For example, Mn dissolution appears to be reduced during cell cycling when manganese oxide spinel is mixed with $LiNi_{0.8}Co_{0.2}O_2$ in certain proportions compared to spinel alone.[42] For this experiment, we milled together spinel $LiMn_2O_4$ with LMO in the ratios indicated in Table 2. Figure S7 shows synchrotron XRD patterns, normalized Mn K-edge hard XAS spectra and Mn L-edge XAS spectra for the various compositions.

Table 2. Summary of the $Li_xMn_yO_z$ target compositions, calculated Mn oxidation states, and the expected discharge capacities based only on Mn redox.

$n(Li_4Mn_2O_5)/n(LiMn_2O_4)$	Composition	Equivalent composition	Calculated Mn oxidation state	Calculated capacity based on Mn redox (mAh/g)
1:0	$Li_4Mn_2O_5$	$Li_{1.6}Mn_{0.8}O_2$	+3	246
8.5:1.5	$Li_{3.55}Mn_2O_{4.85}$	$Li_{1.46}Mn_{0.82}O_2$	+3.075	233
8:2	$Li_{3.4}Mn_2O_{4.8}$	$Li_{1.42}Mn_{0.83}O_2$	+3.1	229
7.5:2.5	$Li_{3.25}Mn_2O_{4.75}$	$Li_{1.37}Mn_{0.84}O_2$	+3.125	223
7:3	$Li_{3.1}Mn_2O_{4.7}$	$Li_{1.32}Mn_{0.85}O_2$	+3.15	220
6.5:3.5	$Li_{2.95}Mn_2O_{4.65}$	$Li_{1.27}Mn_{0.86}O_2$	+3.175	215
6:4	$Li_{2.8}Mn_2O_{4.6}$	$Li_{1.22}Mn_{0.87}O_2$	+3.2	211

All of the XRD patterns were consistent with the disordered rock salt structure of the parent compound (space group *Fm-3m*), with no evidence of residual spinel apparent. Lattice parameters are presented in Table S1. In general, the lattice parameters for the spinel-modified materials are larger than for the parent material and do not vary systematically, contrary to what would be expected from the nominal compositions presented in Table 2. The Mn oxidation state in the blended materials is expected to rise as more spinel is added to the mixtures (average oxidation state of Mn in $LiMn_2O_4$ is +3.5). However, the Mn K-edge XAS data show a shift to lower energy indicating a decrease in the Mn oxidation state for the blends compared to unblended LMO. Similarly, the oxidation state of Mn at the surface is lower for these materials, as the Mn *L*-edge XAS data shows. These observations suggest that the additional energetic milling process used to make the blends resulted in loss of oxygen, resulting in a lowering of the Mn oxidation state below 3+, especially at the surface.

Figure 9 shows voltage profiles for the first few cycles of cells containing unmodified LMO and the spinel-modified electrodes discharged and charged between 4.8-1.5V. As expected, initial capacities decreased as the spinel content rose, although all were still higher than expected based on the calculations in Table 2. Most of the electrodes delivered 250 mAh/g or more initially upon discharge, with a significant fall-off only seen for the material with the highest amount of spinel (6:4 LMO:spinel). In addition, the first cycle coulombic efficiencies increased proportionally with the spinel content. Most significantly, the capacity retention also improved for cells containing the electrodes made with more spinel. This is most clearly seen in Figure S8, which plots normalized capacity *vs* cycle number for the various cells. The best material overall, considering these three factors (initial capacity, first cycle coulombic efficiency, and capacity retention) appears to be the one with nominal composition $Li_{1.27}Mn_{0.86}O_2$ (6.5:3.5 LMO:spinel), designated LMO-*s* hereafter.
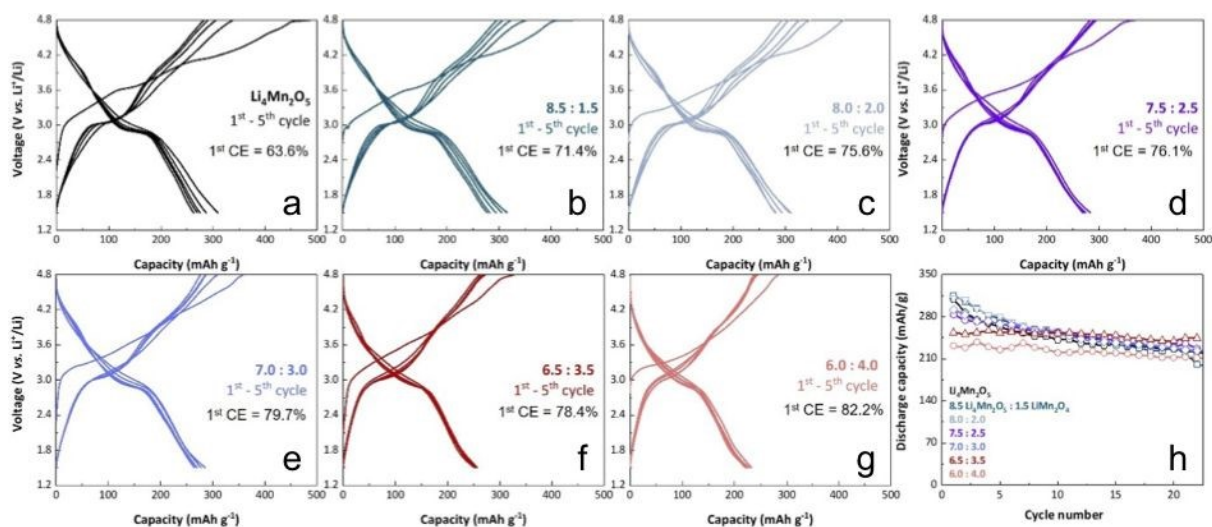
Figure 9. (a-g) Charge and discharge voltage profiles and (h) discharge capacities of Li$_x$Mn$_y$O$_z$ electrodes cycled within a 4.8 – 1.5 V range at C/20 rate.

While LMO-*s* has somewhat lower capacity than the parent LMO compound initially, it cycles better regardless of the voltage limits used, and has better rate capability (Figure S9). Figure S10 also shows that the cell with LMO-s has much improved Coulombic efficiency over that with LMO, especially in the initial five cycles, indicative of its better reversibility.   It outperforms the unmodified LMO in terms of capacity after about 10-25 cycles, depending on the current density used (Figures S9c and S9d). Extended cycling at different rates and between different voltage limits on cells containing LMO-*s* cycled at slightly elevated temperatures (30°C) are shown in Figure S11. The improved capacity retention was maintained over 80-150 cycles.

Interestingly, although the voltage profiles of LMO-*s* appear to change less with cycling than those of unmodified LMO in Figures 9a and 9f, the evolution appears to depend not only on the voltage window used but also on cycling rate (Figures S12-S14), suggesting a dynamic cycling-induced structural rearrangement. The use of a higher charge limit of 4.8 V exacerbates voltage profile evolution more than lower charge limits of 4.5 V or 4.2 V, leading to the development of a plateau-like feature near 4V as indicated by the arrow in Figure S12. The voltage profiles of cells cycled at slower rates appear to evolve more rapidly than those of cells cycled at faster rates. This implies that these structural changes are kinetically limited and may be managed during early cycles through a conditioning process. Galvanostatic intermittent titration technique (GITT) experiments performed at the 1st, 10th, and 25th cycles clearly indicate changes in the LMO-*s* electrode kinetics with cycling. The non-ohmic voltage loss upon discharge, especially before the capacity reaches 50 mA/g, is noticeably reduced at the 25th cycle (Figure S15). Similar voltage profile evolutions were reported for other cation-disordered rocksalt cathodes like Li$_{1.1}$Mn$_{0.8}$Ti$_{0.1}$O$_{1.9}$F$_{0.1}$,[43] and have been attributed to the formation of a partially ordered disordered rocksalt phase with a *β'*-LiFeO$_2$-type arrangement.
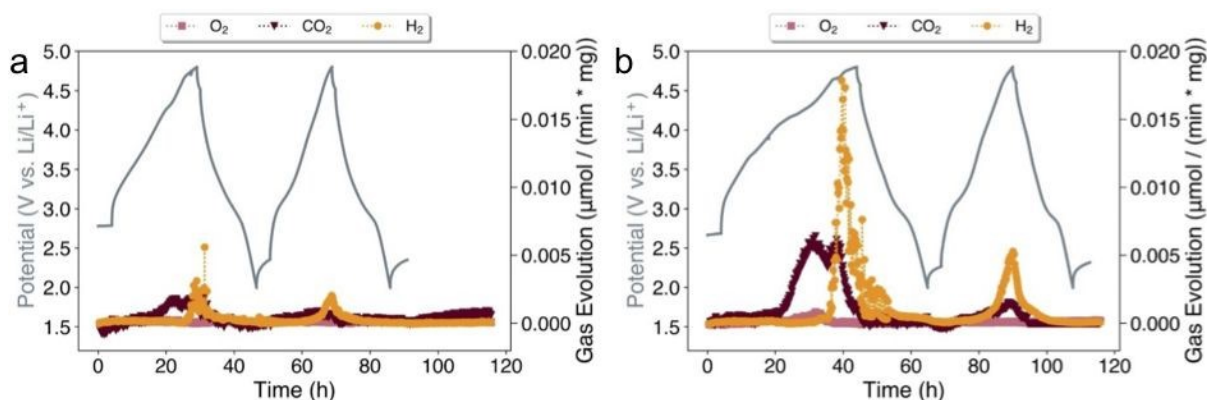
Figure 10. Differential electrochemical mass spectrometry (DEMS) profiles for gas evolution from cells made with (a) LMO-*s* and (b) LMO during the initial two cycles between 4.8 and 2.0 V at a current rate of C/10. The data points at ~ 30 h in (a) and at ~ 45 h in (b) deviating from the neighboring points could originate from signal fluctuations.

In order to gain insights into the origins of the improved electrochemical properties of LMO-*s*, we conducted differential electrochemical mass spectrometry experiments on two different cells; one containing LMO and the other containing LMO-*s* (Figure 10 and Table S2). During the first electrochemical cycle, large amounts of O_2, CO_2, and H_2 gases are detected near the top of charge for the LMO cell. In contrast, much less gas is evolved on the first cycle for the LMO-*s* cell, and, significantly, no oxygen is detected at all. In both cases, smaller amounts of H_2 and CO_2 gases evolved on the second cycle, and oxygen is no longer detected. This observation implies that the oxygen activity in LMO-*s* is much lower than in LMO, perhaps due to the additional processing for the former, which resulted in oxygen loss prior to incorporation in cells. Carbon dioxide may arise from decomposition of adventitious Li_2CO_3 on particle surfaces or from the electrolytic solution, while hydrogen gas may be produced by crosstalk between electrodes; *i.e.*, protic decomposition products produced upon oxidation of components in the electrolytic solution travel to the anode and are reduced there. (This may account for the delay in detecting hydrogen gas compared to the other gases). The lower activity of oxygen in LMO-*s* mitigates side reactions at the top of charge and accounts for the better cycling that is observed. While oxygen loss during processing can partially explain this, the lower lithium content and higher Mn content of LMO-*s* compared to LMO may also play roles. For example, the better cycling behavior of $Li_{1.1}Mn_{0.7}Ti_{0.2}O_2$ compared to $Li_{1.3}Mn_{0.4}Ti_{0.4}O_2$ has been attributed to the higher Mn content and the accompanying changes in electronic structure that raise the O-O aggregation barrier and discourage oxygen release during cycling.[44]

Figure 11 shows Mn K-edge XAS spectra of LMO and LMO-*s* electrodes harvested from cells cycled the indicated number of times and stopped in the discharged state. In the case of the LMO electrodes, there is a shift to lower energies after one or five cycles between 4.8-2.5V (Figure 12b), indicating that the average Mn oxidation state at the end of discharge decreased. There is much less shift observed for the LMO-*s* electrode cycled under the same conditions (Figure 12a). The differences between electrodes subjected to prolonged cycling between 4.8-2.0V (Figures 12c and d) are even more stark. The Mn oxidation state of the LMO-*s* electrodes in the discharged state

appears to be relatively stable even after 114 cycles, whereas it decreased markedly during initial cycles in the LMO electrodes and only stabilized thereafter. This provides additional evidence that the LMO-*s* material is less reactive at high states-of-charge than LMO. In the case of the latter, the initial loss of oxygen exacerbates side reactions with the electrolytes, which in turn cause reduction of Mn at the top of charge. This causes over-reduction of Mn below 3+ upon the subsequent discharge and may also contribute to Mn dissolution.[45,46]
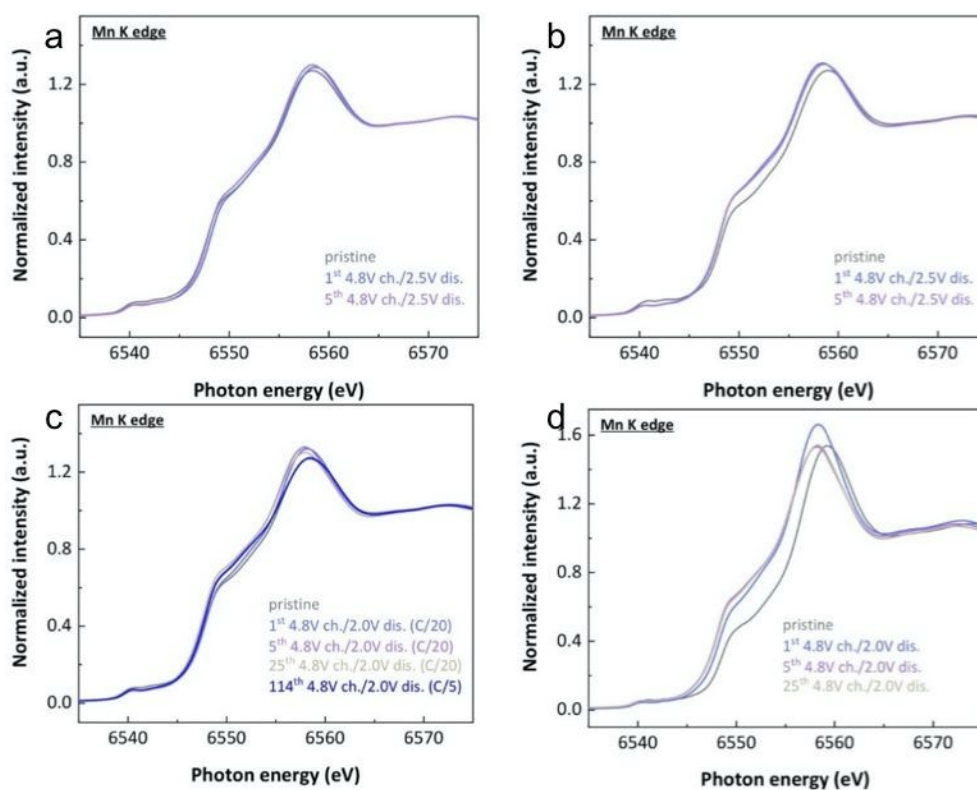
Figure 11. Normalized Mn *K*-edge hard XAS spectra of (a, c) LMO-*s* and (b, d) LMO electrodes discharged respectively to (a, b) 2.5 V and (c, d) 2.0 V, and cycled the indicated number of cycles. All the electrodes were cycled at current rate C/20.

For the surface Mn state characterizations, the Mn L-edge XAS data on discharged, charged and cycled LMO-*s* electrodes is shown in Figure S16. As expected, Mn is oxidized to the tetravalent state as clearly indicated by the spectral lineshape.[36] Discharging the electrodes to lower voltages leads to increasing amounts of Mn^{2+} on the surface (Figure S16a); however, the overall surface Mn^{2+} formation seems to be weaker than for LMO (Figure 8), which is also consistent with the hard XAS observations, in contrast to that of LMO.

Overall, the addition of spinel during processing of LMO electrode materials appears to have a number of beneficial effects. Although the changes in nominal composition caused by the addition should result in reduced gravimetric capacity, the effect is lower than expected except at

high spinel contents. Cells containing optimized spinel-modified electrodes (LMO-*s*) exhibited less gas evolution upon initial cycles, due to lowered oxygen activity, which ameliorates side reactions with electrolyte. This results in improved cycling for cells containing optimized spinel-modified cathodes and less tendency towards Mn over-reduction. Rate capability is also improved in these cells. Although structural changes and surface Mn^{2+} formation still occur upon cycling, they are rate and voltage-limit dependent so it may be possible to manage them by initial conditioning to ensure major changes are limited to early cycles.

Conclusions

The anomalously high capacities observed in cells containing "$Li_4Mn_2O_5$" under some cycling conditions can be explained entirely by decomposition of Li_2O and/or Li_2CO_3 upon initial charge, followed by over-reduction of Mn upon subsequent discharge. RIXS experiments show no evidence of reversible oxygen redox, suggesting no reversible reduction of the oxidized oxygen during initial charge, and Mn redox ($Mn^{2+}/Mn^{3+}/Mn^{4+}$) dominates as the main charge contributor during the following cycles for all conditions studied here. This agrees with previous results on other oxide electrode materials that contain only manganese as the transition metal (*e.g.*, Li_2MnO_3). Irreversible release of oxygen occurs during the first charge, leading to clear spectroscopic evidence of large amounts of Mn^{2+} formation on the surface, apparent loss of capacity, and increased cell resistance upon cycling. Manganese dissolution also occurs. The addition of spinel during the reactive ball-milling process used during synthesis results in electrode materials with significantly better cycling and rate capability characteristics. This can be attributed to lower reactivity at high states-of-charge and less tendency to manganese over-reduction upon cycling.

Author Contributions

W. Y. and J.A. carried out synthesis and electrochemical and synchrotron characterization of materials and analyzed data. E.A.K. performed and analyzed DEMS experiments under the supervision of B.D.M. C. D. performed XPS experiments under the supervision of J. J. U. Z.Z. and W.Y. carried out mRIXS experiments and analyzed the results. MMD supervised the project. W.Y. and MMD wrote the original draft, and all authors reviewed and edited the manuscript.

Conflict of interest

The authors declare no conflicts of interest.

Acknowledgements

Data availability

The data that support the findings of this study are available upon request.

References

1. G. N. Newton, L.R. Johnson, D.A. Walsh, B. J. Hwang, and H. Han, *ACS Sust. Chem. & Eng.*, 2021, **9**, 6507.

2. S. Ahmed, S. E. Trask, D. W. Dees, P.A. Nelson, W. Lu, A.R. Dunlop, B. J. Polzin, and A. N. Jansen, *Journal of Power Sources* 2018, **403**, 56.

3. M. M. Thackeray, W.I. F. David, P.G. Bruce, and J.B. Goodenough, *Mater. Res. Bull.*, 1983, **18**, 461.

4. J. R. Croy, M. Balasubramanian, K. G. Gallagher, and A. Burrell, *Acc. Chem. Res.*, 2015, **48**, 2813.

5. R. J. Clement, Z. Lun and G. Ceder, *Energy & Environ. Sci.* 2020, **13**, 345.

6. H. Li, R. Fong, M. Woo, H. Ahmed, D.-H. Seo, R. Malik and J. Lee*, Joule*, 2022, **6**, 53.

7. D. Chen, W.H. Kan, and G. Chen, *Adv. Energy Mater.*, 2019, **9**, 1901255.

8. M. Freire, N. V. Kosova, C. Jordy, D. Chateigner, O. I. Lebedev, A. Maignan, and V. A. Pralong, *Nat Mater.*, 2016, **15,** 173.

9. M. Freire, M. Diaz-Lopez, P. Bordet, C.V. Colin, O.I. Lebedev, N.V. Kosova, C. Jordy, D. Chateigner, A. L. Chuvilin, A. Maignan, and V. Pralong, *J. Mater. Chem. A*, 2018, **6**, 5156.

10. N. Yabuuchi, M. Takeuchi, M. Nakayama, H. Shiiba, M. Ogawa,K. Nakayama, T. Ohta, D. Endo, T. Ozaki, T. Inamasu, K. Sato, and S. Komaba, *Proc. Natl. Acad. Sci. USA*, 2015, **112**, 7650.

11. J. Qian, Y. Ha, K. P. Koirala, D. Huang, Z. Huang, V.S. Battaglia, C. Wang, W. Yang, and W. Tong, *Adv. Funct. Mater.*, 2023, **33**, 2205972.

12. J. Ahn, Y. Ha, R. Satish, R. Giovine, L. Li, J. Liu, C. Wang, R.J. Clement, R. Kostecki, W. Yang, and G. Chen, *Adv. Energy Mater.*, 2022, **12**, 202200426.

13. D.-H. Kwon, J. Lee, N. Artrith, H. Kim, L. Wu, Z. Lun, Y. Tian, Y. Zhu, and G. Ceder., *Cell Reports Phys. Sci.*, 2020, **1**, 100187.

14. L. Li, Z. Lun, D. Chen, Y. Yue, W. Tong, G. Chen, G. Ceder, and C.Wang,. *Adv. Funct. Mater.* 2022, **34**, 2106256.

15. L. Li, J. Ahn, Y. Yue, W. Tong, G. Chen, and C. Wang, *Adv. Mater.*, 2022, **34**, e2106256.

16. X. Fan and C. Wang, *Chem. Soc. Rev.* 2021, **50**, 10486.

17. Y. Chen, Q. He, Y. Mo, W. Zhou, Y. Zhao, N. Piao, C. Liu, P. Xiao, H. Liu, B. Li, S. Chen, L. Wang, X. He, L. Xing, and J. Liu, *Adv. Energy Mater.* 2022, **12**, 2201631.

18. F. Lin, Y. Liu, X. Yu, L. Cheng, A. Singer, O. G. Shpryko, H. Xin, N. Tamura, C. Tian, T.-C. Weng, X.-Q. Yang, Y. S. Meng, D. Nordlund, W. Yang, and M. Doeff, *Chem. Rev.* 2017, **117**, 13123.

19. B.D. McCloskey, D.S. Bethune, R.M. Shelby, G. Girishkumar, and A. C. Luntz, *J Phys. Chem. Lett.* 2011, **2**, 1161.

20. H. Li, I. Roy, M. Starczewski, J. Freeland, and J. Cabana, *J. Phys. Chem. C*, 2023, **127**, 7913.

21. N. P. W. Pieczonka, Z. Liu, P. Lu, K.L. Olson, J. Moote, B.R. Powell, and J.-H. Kim, *J. Phys. Chem. C*, 2013, **117**, 15947.

22. R. Sahore, D.C. O'Hanlon, A. Tornheim, C.-W. Lee, J. C. Garcia, H. Iddir, M. Balasubramanian, and I. Bloom, *J. Electrochem. Soc.* 2020, **167**, 020513.

23. Y. Zhang, A. Hu, D. Xia, S. Hwang, S. Sainio, D. Nordlund, F. M. Michel, R.B. Moore, L. Li, and F. Lin, F., Operando Characterization and Regulation of Metal Dissolution and Redeposition Dynamics near Battery Electrode Surface. *Nat. Nanotechnol.,* 2023 https://doi.org/10.1038/s41565-023-01367-6.

24. R. Satish, L. Wichmann, J.J. Crafton, R. Giovine, L. Li, J. Ahn, Y. Yue, W. Tong, G. Chen, and C. Wang, *ChemElectroChem*, 2021, **8,** 3982.

25. C. Wang, L. Xing, J. Vatamanu, Z. Chen, G. Lan, W. Li, and K. Xu, *Nat Commun.*, 2019, **10**, 3423.

26. C. Zhan, T. Wu, J. Lu, and K. Amine, *Energy & Environ. Sci.*, 2018, **11**, 243.

27. J. R. Croy, D. Kim, M. Balasubramanian, K. Gallagher, S.-H. Kang, and M. M. Thackeray, *J.Electrochem. Soc.*, 2012, **159**, A781.

28. U. Bergmann, P. Glatzel, and S.P. Cramer, *Microchem. J.*, 2002, **71**, 221.

29. J. Alvarado, C. Wei, D. Nordlund, T. Kroll, D. Sokaras, Y. Tian, Y. Liu, and M. M. Doeff, *Mater. Today*, 2020, **35**, 87.

30. M. Diaz-Lopez, Y.Joly, M. Freire, C. Colin, O. Proux, V. Pralong, and P. Bordet, *J.. Phys. Chem. C*, 2018, **122**, 29586.

31. C. Tian, D. Nordlund, H. Xin, Y. Xu, Y. Liu, D. Sokaras, F. Lin, and M. Doeff, *J. Electrochem. Soc.*, 2018, **165**, A696.

32. R. Qiao, Y.D. Chuang, S. Yan, and W. Yang, *PLoS One*, 2012, **7**, e49182.

33. S. Roychoudhury, R. Qiao, Z. Zhuo, Q. Li, Y. Lyu, J.-H. Kim, J. Liu, E. Lee, B.J. Polzin, J. Guo, S. Yan, Y. Hu, H. Li, D. Prendergast, and W. Li, *Energy & Environ. Mater.*, 2020, **4**, 246.

34. K. Dai, J. Wu, Z. Zhuo, Q. Li, S. Sallis, J. Mao, G. Ai, C. Sun, Z. Li, W.E. Gent, W.C. Chueh, Y.D. Chuang, R. Zeng, Z-X. Shen, F. Pan, S. Yan, L.F.J. Piper, Z. Hussain, G. Liu, and W. Yang., *Joule*, 2019, **3**, 518.

35. K. McColl, R.A. House, G.J. Rees, A. G. Squires, S.W. Coles, P.G. Bruce, B.J. Morgan, and M. S. Islam, *Nature Commun.*, 2022, https://doi.org/10.1038/s41467-022-32983-w

36. R. Qiao, T. Chin, S.J. Harris, S. Yan, and W. Yang, *Current Appl. Physics*, 2013, **13**, 544.

37. J. Wu, Z. Zhuo, X. Rong, K. Dai, Z. Lebens-Higgins, S. Sallis, F. Pan, L. F. J. Piper, G. Liu, Y.-D. Chuang, Z. Hussain, Q. Li, R. Zeng, Z.-X. Shen, and W. Yang, *Sci.Adv.*, 2020, **6,** DOI: 10.1126/sciadv.aaw3871.

38. R. Qiao, K. Dai, J. Mao, T.-C. Weng, D. Sokaras, D. Nordlund, X. Song, V.S. Battaglia, Z. Hussain, G. Liu, and W. Yang, *Nano Energy*, 2015, **16**, 186.

39. Z. Zhuo, K. Dai, R. Qiao, R. Wang, J. Wu, Y. Liu, J. Peng, L. Chen, Y.-D. Chuang, F. Pan, Z.-X. Shen , G. Liu, H. Li, T.P. Devereaux, and W. Yang, *Joule*, 2021, **5**, 975.

40. R. D. Shannon, *Acta Cryst.*, 1976, **A32**, 751.

41. S. B. Chikkannanavar, D. M. Ernardi, and L. Liu, *J. Power Sources*, 2014, **248**, 91.

42. T. Numata, C. Amemiya, T. Kumeuchi, M. Shirakata, and M. Yonezawa, *J. Power Sources,* 2001, **97-98**, 358.

43. J. Ahn, R. Giovine, V.C. Wu, K. P. Koirala, C. Wang, R.J. Clement, and G. Chen, *Adv. Mater.*, 2023, **13**, 2300221.

Journal of Materials Chemistry A Accepted Manuscript

44. K. Zhou, Y. Li, S. Zheng, M. Zhang, C. Zhang, C. Battaglia, H. Liu, K. Wang, P. Yan, J. Liu, and Y. Yang., *Energy Storage Materials*, 2021, **43**, 275.

45. J. M. Tarascon, W.R. McKinnon, F. Coowar, T.N. Bowmer, G. Amatucci, and D. Guyomard, *J. Electrochem. Soc.*,. 1994, **141**, 1421.

46. S. Komaba, T. Itabashi, T. Ohtsuka, H. Groult, N. Kumagai, B. Kaplan, and H. Yashiro, *J. Electrochem. Soc.*, 2005, **152**, A937.